

# L'ADROIT – A spaceborne ultraviolet laser system for space debris clearing

Claude R. Phipps\*

Photonic Associates, LLC, 200A Ojo de la Vaca Road, Santa Fe, NM 87508, USA



## ARTICLE INFO

### Article history:

Received 27 May 2014

Received in revised form

6 August 2014

Accepted 8 August 2014

Available online 19 August 2014

### Keywords:

Space debris removal

Laser ablation

Laser-produced plasma

Neodymium laser

Ytterbium laser

Third harmonic

## ABSTRACT

Small (1–10 cm) debris in low Earth orbit (LEO) are extremely dangerous, because they spread the breakup cascade. Pulsed laser active debris removal using laser ablation jets on target is the most cost-effective way to re-enter the small debris. No other solutions address the whole problem of large (~100 cm, 1 t) as well as small debris. Physical removal of small debris (by nets, tethers and so on) is uneconomical because of the energy cost of matching orbits. In this paper, we present a completely new proposal relative to our earlier work. This new approach uses rapid, head-on interaction in 10–40 s rather than 4 minutes, using 20–40 kW bursts of 100 ps, 355 nm UV pulses from a 1.5 m diameter aperture on a space-based station in LEO. The station employs “heat-capacity” laser mode with low duty cycle to create an adaptable, robust, dual-mode system which can lower or raise large derelict objects into less dangerous orbits, as well as clear out the small debris in a 400-km thick LEO band. Time-average laser optical power is less than 15 kW. The combination of short pulses and UV wavelength gives lower required fluence on target as well as higher momentum coupling coefficient. An orbiting system can have short range because of high interaction rate deriving from its velocity through the debris field. This leads to much smaller mirrors and lower average power than the ground-based systems we have considered previously. Our system also permits strong defense of specific assets. Analysis gives an estimated cost less than \$1 k each to re-enter most small debris in a few months, and about 280 k\$ each to raise or lower 1-ton objects by 40 km. We believe it can do this for 2000 such large objects in about four years. Laser ablation is one of the few interactions in nature that propel a distant object without any significant reaction on the source.

© 2014 IAA. Published by Elsevier Ltd. All rights reserved.

## 1. Background

As the movie “Gravity” dramatically illustrated [1], the instability predicted by Kessler and Cour-Palais [2] is propagated between big objects by small debris. The instability has now reached the point where collisional cascades threaten the use of LEO space. The small ones are a significant threat. With relative impact velocities of order 15 km/s and mass areal density of order 1 kg/m<sup>2</sup>, a 2 cm,

300 mg piece of small debris has a kinetic energy density of 113 MJ/kg, 23 times that of dynamite. Its kinetic energy is 83 times that of a 9 mm Luger round.

While improved debris tracking and orbit prediction can temporarily improve threat avoidance via maneuvering [3,4], effective debris-clearing strategies will be necessary. For very large objects like the 8-ton ENVISAT, an effective maneuver is to lower or raise it about 40 km, resulting in less collision probability as well as less perceived risk [see Section 3.2].

Four cataloged events have now occurred in which a debris collision terminated an active satellite. Thirty-five cataloged satellite breakups are of unknown cause, and

\* Tel.: +1 505 466 3877.

E-mail address: [crrhipps@photonicassociates.com](mailto:crrhipps@photonicassociates.com)

many of these are surely due to collisions with untracked debris. However, the main urgency is to mitigate future risks. More than one hundred 1400-kg Cosmos 3 M third stages with up to 300 kg of residual propellant are still in LEO and medium-Earth orbit (MEO), waiting to spontaneously explode, as they have five times. Based on [5], we estimate the cumulative probability of ENVISAT's debris-induced failure at 8%/decade. Its catastrophic failure would jeopardize use of sun-sync orbits, and threaten the region around 766 km altitude in the long term. It will take a decade to implement an effective debris removal system, so now is the time to begin. Large debris must be removed. They are the main source of additional debris when hit. Small debris must also be removed. They are much more numerous and so are the main threats because of the additional debris they create when they collide with a larger object. These were the main conclusions of a 45-student study at the International Space University [6]. The chance that small debris will strike a large LEO space asset is 45 times as high as the hazard from large objects [7]. Table 1 summarizes these conclusions.

**2. Proposed solutions**

*2.1. Absorbing or changing orbits of debris*

Solutions that have been proposed for large objects include chasing and grappling, attaching electrodynamic tethers, deploying nets, and deploying clouds of frozen mist, gas or blocks of aerogel in the debris path to slow the debris. Some of these are difficult to implement, costly and address only one or a few objects at a time. For example, an aerogel “catcher's mitt” designed to clear the debris in two years would require a slab 50 cm thick and 13 km on a side. Such a slab would weigh 80 kt, cost \$1 T to launch (Table 2), and require a steady 12 kN average thrust to oppose orbital decay of the slab against ram pressure, even in an elliptical orbit [8].

**Table 1**  
LEO debris categories.

LEO Debris	Small	Large
Size (cm)	1–10	10–1000
Accessible Targets	100 k	2.2 k
Numerical Ratio	45	1
Characteristic	Main threat	Main source

**Table 2**  
Examples of proposed LEO debris clearing systems.

Applicable to ⇒ Approach ↓	Large Debris	Small Debris	Disadvantages	Advantages
Electrodynamic Tethers	Yes	No	Large Δv to reach successive objects, ~17M\$/object	Good for few, large objects
Aerogel Blocks	Yes	Yes	1T\$ cost to launch & maintain, Clutters space	Shield individual objects
Nets	Yes	No	Large Δv to reach successive objects, ~17M\$/object	Good for few, specific objects
Groundbased Laser Active Debris Removal (LODR, ORION)	Yes	Yes	Weather, self-focusing, stimulated Raman scattering, turbulence, large telescopes, adaptive optics	Good for all, low cost per small object
Spacebased Laser Active Debris Mitigation (“L'ADROIT,” this paper)	Yes	Yes	Launch cost; difficult to repair	Good for all, small optics, very low cost per small object

Few concepts have progressed to the point where accurate costs can be calculated, but Bonnal [9] has estimated a cost of 13–17 M\$ per object for deorbiting large targets. Any mechanical solution will involve a comparable Δv from Earth, so we take this estimate as representative of removal cost per large item with mechanical methods.

*2.2. Laser interaction categories*

At low intensities below the ablation threshold, lasers have been proposed to divert debris through light pressure [10]. In this case, the proposed hardware arrangement will deliver at most a few times the intensity of the sun to the debris, and that only during a few minutes' time while the debris passes above the laser site, rather than all day. Sunlight produces a larger time-integrated effect. This method does not effectively address the debris growth problem.

Laser ablation is more effective by several orders of magnitude. But, at the focal plane intensity required for continuous (CW) laser ablation, the necessary laser power is daunting [see Section 4.3], and splashing is likely.

Pulsed laser ablation is an optimum use of laser average power because the ablation impulse and efficiency can be optimized for each type of target material, and removes nm of material per pulse.

A NASA headquarters concept validation study [11] concluded that it is feasible to use pulsed lasers to remove essentially all dangerous orbital debris in the 1–10 cm range between 400 and 1100 km altitude within two years, and that the cost of doing so would be modest compared to that of shielding, repairing, or replacing high-value spacecraft that would otherwise be lost to debris impact. We believe this is still true, and that the time for action has arrived.

**3. Laser debris removal system design**

*3.1. System goals*

Reasonable goals for a laser debris removal (LDR) system are that it should remove small debris, as well as reduce the threat of large debris by raising/lowering them into a less hazardous orbit, work fast, have the best cost per debris object and avoid the perceived risks associated with LDR. These are: unpredictable re-entry location on

the ground for large objects that might survive re-entry, unintended dazzling of spaceborne sensors and injuring people on the ground. The design we present in this paper will achieve these goals.

### 3.2. L'ADROIT system concept

We call the concept we introduce in this paper Laser Ablative Debris Removal by Orbital Impulse Transfer. It achieves the system goals in six specific ways.

First, we will lower or raise large objects rather than attempting to re-enter them, until we have demonstrated precision operation of our system, to eliminate one of the perceived risks. Lowering ENVISAT by 40 km will reduce the threat to it by a factor of four [12].

Second, we use 100 ps ultraviolet pulses at the 3rd harmonic of neodymium (Nd) at 355 nm or, possibly, that of ytterbium (Yb) at 343 nm. The shorter wavelength and pulsewidth (compared to the 1.06  $\mu\text{m}$ , 10 ns pulses we used in previous work) give a factor of 9 less fluence ( $\text{J}/\text{cm}^2$ ) required on target to produce optimum mechanical impulse coupling, and an improved impulse coupling coefficient. Diffraction at 355 nm gives a 3-times-smaller illumination spot for a given range (Section 4.4). Lower fluence on target corresponds to lower laser pulse energy required from the laser. Further, atmospheric attenuation at 355 nm is 0.3/km [13], so that transmission on a tangent path to Earth from space is only  $2.5\text{E}-9$ , preventing eye injuries on the ground. This choice also gives low background illumination and dark, absorptive targets.

Third, we put the system in LEO rather than on the ground, where the orbital sweep velocity gives a comparatively large target access rate with a black background for better target detection. Higher access rate, in turn, permits using much smaller laser range, of order 250 km for small objects, and smaller, lighter optics to project the beam, compared to the groundbased alternative. For large targets, we can use the same optics and larger pulse energy with range of order 600 km, because large targets do not require small illumination spots. In space, we have perfect path transmission, and no scintillation or nonlinear optical effects, so that we can dispense with adaptive optics outside the laser system itself.

Fourth, we interact with small debris head-on to produce re-entry in 10 s (rather than the 4 min intervals used in [7]), with short, high power bursts of pulses with even higher momentary power from a 1.5 m diameter aperture. We do not have to reacquire the small targets after the interaction. For large targets, we use many 40 s interactions over four years to lower/raise all of them, and here we can rely on groundbased tracking for reacquisition.

Fifth, we set a polar, elliptical orbit which will access most LEO debris. Fig. 1 [14] shows us that, on a polar orbit, the azimuth range  $\pm 30^\circ$  will encompass most of the debris. As we remove these, others will fill in the distribution until all are gone.

Sixth, our laser is mainly aimed horizontally. This, together with the UV wavelength eliminates dazzle of reconnaissance sensors, which look down and mostly use infrared wavelengths. Operating head-on into our targets,

rather than up from the ground, also provides a much better momentum exchange geometry.

We will use “heat-capacity” laser mode with low duty cycle to create an adaptable, robust, dual-mode system which can lower or raise large derelict objects into less dangerous orbits, as well as clear out the small debris in a 400-km thick band in LEO. Heat capacity mode means momentarily operating a solid state laser in a mode beyond its continuous capability for heat dissipation in its components, using their thermal capacity, and cooling later. Time-average laser optical power in small target mode is about 2 kW.

Fig. 2 shows that in this polar orbit, typical debris have a 15 km/s velocity relative to our station.

Fig. 3 shows the L'ADROIT system. It is launched into a polar orbit with eccentricity  $e=0.028$ , inclination  $i=90^\circ$ , argument of the periapsis  $\omega=-180^\circ$ , maximum altitude 960 km and minimum altitude 560 km. Altitude at the poles is 760 km. In this orbit, it will eventually intersect the orbits of all debris in the band  $h=760 \pm 200$  km and, at the poles, repeatedly intersect the altitude of many sun-synchronous orbits, especially that of ENVISAT. Its orbit matches the conditions of Figs. 1 and 2.

Fig. 4 shows the components of the system. Two telescopes are used. One is a wide field of view passive acquisition sensor, using daylight scattered from the target to detect its position. On average, a target is in daylight half the time. The telescope is aspheric, with a design described in the next section.

The second is an off-axis Cassegrain with a 6 mrad ( $0.34^\circ$ ) field of view (FOV) which is used to project the laser beam. For acquisition, the laser pulse energy is just 1 J, but for pushing on large targets it can be as large as 3 kJ. This telescope is steered to the position indicated by the passive acquisition sensor, and the focus can be zoomed slightly to match the beam waist diameter and position to the target position as it approaches [15].

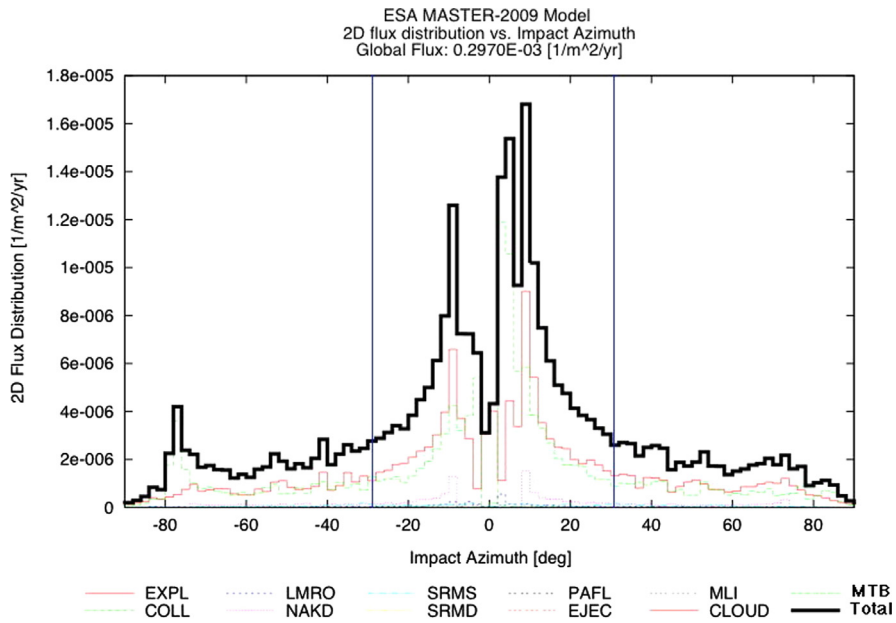
### 3.3. Target access rate

In order to achieve adequate target detection rate, we require a passive sensor with a large FOV. For  $N$  targets uniformly distributed in a band  $\Delta h$  thick at altitude  $h$ , the rate at which a passive detection system with field of view moving at velocity  $v_o$ , range  $z$ , thickness  $\Delta z$ , and field of view  $\Omega$  accesses targets is:

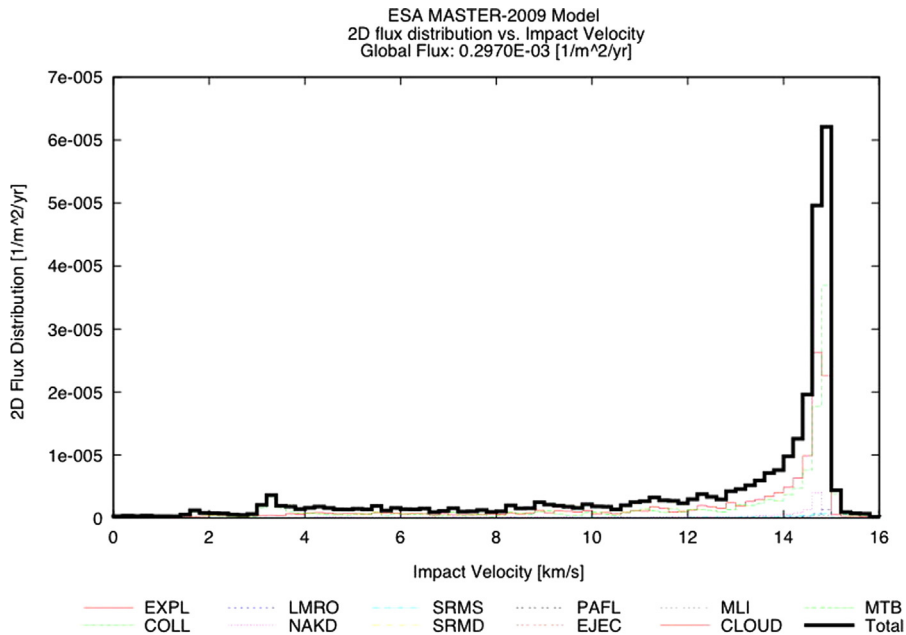
$$dN/N dt = v_o \Omega z^2 \Delta z / [4\pi(R_E + h)^2 \Delta h]. \quad (1)$$

In Eq. (1),  $R_E$  is the Earth's radius.

To obtain a useful access rate for small targets, let alone the less numerous large ones, we found that we needed at least a  $60^\circ$  FOV (0.87 sterad) for the acquisition optic. Fig. 5 shows how this is possible with two computer-generated conic sections obtained by revolving the Figure about the vertical axis [16]. A 1:1 correspondence exists between a position on the array detector and a direction in the field of view. Köse et al. obtained a  $126^\circ$  FOV in their design, much more than we require. This is a modern example of a set of conic sections which gave a  $180^\circ$  FOV in [17]. We chose 72  $\mu\text{rad}$  FOV for one pixel, leading to a 212 Mpixel visible wavelength array with 10 cm diameter.



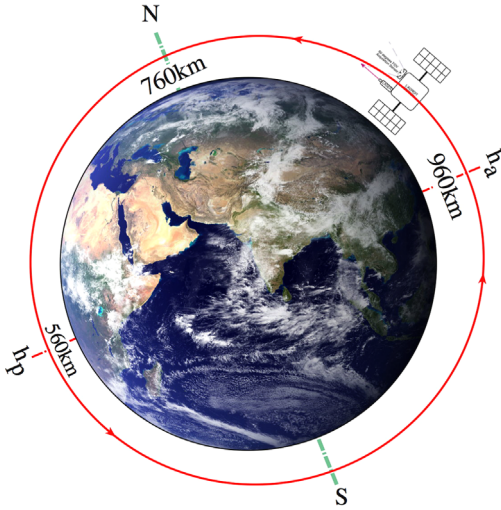
**Fig. 1.** Source-wise and total debris flux for  $d > 1$  cm on an ERS orbit [ $i=98.6^\circ$ ,  $h=773 \times 789$  km], as a function of the impact azimuth  $A$  (class width  $\Delta A=3^\circ$ ) [Results of ESA MASTER-2009 model (H.Krag, DLR 2014), used by permission. See <https://sdup.esoc.esa.int>. Acronyms: EXPL: explosion fragments. LMRO: launch and mission related objects, intact. SRMS: solid rocket motor aluminum oxide slag. SRMD: solid rocket motor aluminum oxide dust. EJEC: hypervelocity impact ejects. CLOUD: fragmentation clouds. MLI: multi layer insulation. COLL: collision fragments. PAFL: paint flakes. MTB: meteoroid background. A majority of the debris is included within a  $\pm 30^\circ$  azimuth relative to the orbiting ADROIT station.



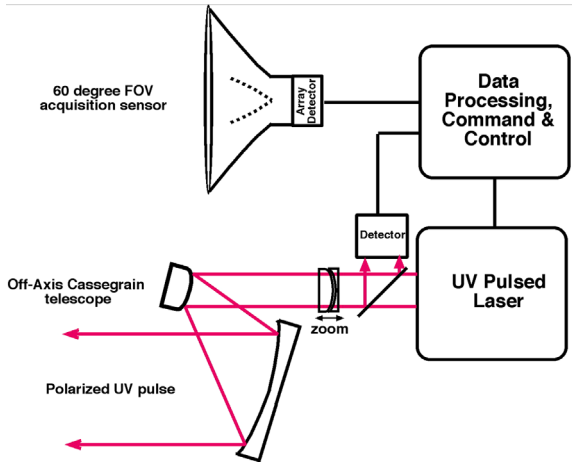
**Fig. 2.** Source-wise and total debris flux for  $d > 1$  cm on an ERS orbit, [ $i=98.6^\circ$ ,  $h=773 \times 789$  km], as a function of impact velocity  $\Delta v$  (class width:  $\Delta v/v=0.25$  km/s) [H.Krag, DLR (2014) update of H. Klinkrad, *Space Debris, Models and Risk Analysis*, Springer Praxis (2006), Fig. 4.4, p. 127] used by permission, acronyms same as for Fig. 1.

Table 3 gives our access rate results for small targets at different ranges. For small debris, we use range  $z=250 \pm 75$  km to combine good acquisition rate ( $\sim 20$ /min), reasonable pulse energy (380 J), spot size larger than all targets (0.22 m) and reasonable transverse angular rate for targets moving within  $\pm 30^\circ$  of our path ( $1.7^\circ/s$ ).

We employ a minimum range of  $z=175$  km to not exceed this maximum transverse angular rate and avoid heroic target tracking rates. Test volume thickness  $\Delta z=150$  km gives 10 s operation time per target approaching at 15 km/s. For this analysis, we assume  $NS=100$  k small debris distributed uniformly within the



**Fig. 3.** L'ADROIT system in orbit. A slightly eccentric polar orbit with 90° inclination covers the altitude range 560–760 km.



**Fig. 4.** Components of the L'ADROIT system. A wide field of view passive acquisition sensor identifies targets using solar illumination. A 355 nm, 6 mrad narrow FOV active acquisition and firing unit tracks the target, obtains returns from it, focuses on it and fires repeatedly to alter its orbit. Because the outgoing pulse is polarized, it passes through the splitter with zero loss, while the return pulse suffers a 50% loss. Only the active telescope is steered. Section 5 provides more details of the design.

altitude band  $\Delta h=400$  km centered on  $h=760$  km. The resulting spatial number density times the swept area times relative velocity  $v=15$  km/s corresponds exactly to the flux shown in Fig. 1 added up across the azimuth bins between  $\pm 30^\circ$ . We assume  $NL=2000$  large debris in the band [7]. Section 5 provides more detail on pointing accuracy.

Table 4 gives access rate results for large targets. We see that a range  $z=600 \pm 300$  km is a good choice to combine good acquisition rate rate ( $\sim 1.5/\text{min}$ ), reasonable pulse energy (2 kJ), laser spot diameter appropriate for all targets ( $\sim 0.5$  m) and reasonable transverse angular rate ( $0.9^\circ/\text{s}$ ). Test volume thickness  $\Delta z=600$  km gives 40s operation time per target approaching at 15 km/s.

### 3.4. Target passive acquisition in daylight

Access is not acquisition. Acquisition implies not only target access, but achievement of adequate signal to background ratio ( $S/B$ ) and adequate photoelectron number  $N_{pe}$  per detector array pixel. We take  $N_{pe}=10$ . Tables 5 and 6 show these results for small and large targets acquired passively. Values used for these calculations are given in [7]. In those tables,  $R_{diff}$  is the diffuse reflectivity (per steradian).

The values we used for background and source irradiance  $B\lambda$  and  $I_\lambda$  are given in the header of Table 6 [18–20].  $I_\lambda$  is source brightness due to solar radiation, and  $\Delta t$  is the target residence time on one pixel. We see that all cases give adequate  $N_{pe}$  and  $S/B$  ratio, even at 900 km range, so long as the debris are in sunlight. Relevant relationships are [7]:

$$S/B = R_{diff} I_\lambda / B_\lambda (d/d_{sp})^2 \quad (2)$$

$$N_{pe} = \frac{d_{sp} \eta_e \pi I_\lambda \Delta \lambda}{16 \nu_\perp z^2 (hc/\lambda)} (d D_b \sqrt{R_{diff}})^2 \quad (3)$$

In Eq. (3), the parameters are photon energy  $hc/\lambda$ , target velocity  $\nu_\perp$  transverse to the field of view (which sets the exposure time per pixel), detector photoelectric efficiency  $\eta_e$ , viewing spot size of one pixel  $d_{sp}$  and optical bandwidth  $\Delta \lambda$ . For example, with 250 km range,  $d_{sp}=18$  m. In the visible, we take  $\eta_e=75\%$ . At the extreme range  $z=900$  km used for large targets,  $d_{sp}=65$  m. Having located a target's transverse position passively with solar illumination to within this accuracy, we then switch to active acquisition to refine the position further.

### 3.5. Target active acquisition

The active array sensor is a  $3000 \times 3000$  pixel array with total FOV 6 mrad and  $2 \mu\text{rad}$  FOV per element. At 250 km range, one element has 25 cm resolution. In active acquisition, we steer the Cassegrain telescope shown in Fig. 4 until it points in the direction indicated by an element of the Fig. 5 passive acquisition sensor, and refine its pointing until it follows the track indicated by the acquisition array. When the track is stabilized, we send a train of 1 J, 355 nm pulses to the target. The laser is now commanded to fire at progressively increasing energy per pulse, its pointing direction optimized and its focal spot minimized until we see the blue flash of plasma on the target. During a high power burst, we will be able to verify target position along the beam to  $\pm 7.5$  mm, so we will know when we have changed its velocity enough for reentry or, if we are making its path less desirable, to cease firing. Then, we move on to the next target.

Tables 7 and 8 give our results at two ranges, for the return from a 1 J laser pulse. A narrowband filter helps provide the signal to background ratios listed. In the Table, we assume range gating, that is, gating the detector array to respond only during the period  $\Delta z/c$  during which a target signal return will be seen. More array elements would give more precision, with even more  $S/B$  ratio. From the last column in Tables 7 and 8, the benefit of a space background is very clear. We note that, in [7] and [11], we

**Table 3**

Small target access rate and required pulse energy for various ranges.

Range (km)	Test volume $A \cdot \Delta z$ (km <sup>3</sup> )	Target number in test volume	Targets accessed number/min	Max transverse rate deg/s	Single pixel projection at target $d_s$ (m)	Required pulse energy $W$ (J)
175	3.98E+06	1.6	9	2.46	0.16	188
250	8.12E+06	3.2	19	1.72	0.22	380
325	1.37E+07	5.4	32	1.32	0.29	630
500	3.25E+07	12.7	76	0.86	0.43	1410

Assumed number of small targets  $N=100k$ . Altitude band  $\Delta h = 400km$ ,  $h = 760km$ . Test volume thickness  $\Delta z$  (small targets) = 150km.  $A$ =swept area  $\Omega z^2$ . The last column gives pulse energy required to make a plasma and achieve optimum coupling at given range. "Required pulse energy" is explained in Section 4.

**Table 4**

Large target access rate and required pulse energy for various ranges.

Range (km)	Test volume $A \cdot \Delta z$ (km <sup>3</sup> )	Target number in test volume	Targets accessed number/min	Max transverse rate deg/s	Single pixel projection at target $d_s$ (m)	Required pulse energy $W$ (kJ)
300	4.68E+07	0.37	0.55	1.43	0.26	540
600	1.87E+08	1.01	1.52	0.86	0.54	1950
750	2.92E+08	1.46	2.19	0.72	0.61	2850
900	4.21E+08	3.29	4.93	0.48	0.70	3790

As in Table 3, but assumed number of large targets  $N=2k$ , altitude band  $\Delta h = 400km$ ,  $h = 760km$ , test volume thickness  $\Delta z = 600km$ . Despite lower number, much larger test volume still gives reasonable access rate for large targets.

**Table 5**

Photon Budget, Passive Daylight Acquisition:  $S/B$  and  $N_{pe}$  ( $\lambda=550nm$ , 250km range) [ $I_i=1000 Wm^{-2}sr^{-1} \mu m^{-1}$ ,  $B_i=2.7 \mu Wm^{-2}sr^{-1} \mu m^{-1} R_{diff}=0.25$ ,  $D_b=1.5m$ ,  $\Delta t = d_{sp}/V_{perp}=2.4ms$ , pixel FOV = 72 $\mu rad$ ,  $d_{sp}=18m$ , array FOV<sup>1</sup> = 1.05rad.

Debris $d$ (m)	Aperture $D_b$ (m)	$D_b d \sqrt{R}$	$N_{pe}$ /pixel	$S/B$
1	1.5	0.75	8.81E+06	2.86E+05
0.3	1.5	0.225	7.92E+05	2.57E+04
0.05	1.5	0.038	2.20E+04	7.14E+02
0.01	1.5	0.008	8.81E+02	2.86E+01

Note: This is a 212 Mpixel VIS detector array array, 10cm dia.

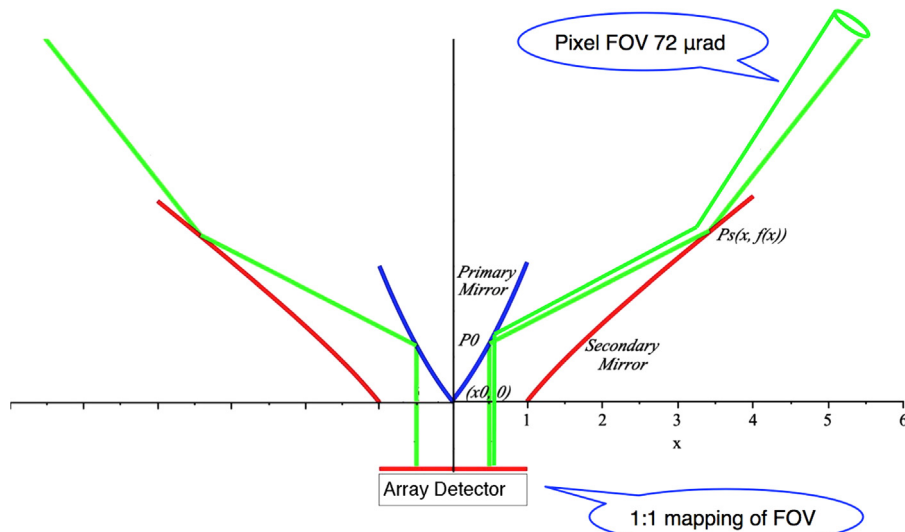


**Fig. 5.** The wide field of view optic made from conic sections used in the passive acquisition system. Adapted from E. Köse and R. Perline (2014), "Double-mirror catadioptric sensors with ultrawide field of view and no distortion," *Appl. Opt.* 53, 528–536, Fig. 6 [used by permission].

**Table 6**

Photon Budget, Passive Daylight Acquisition:  $S/B$  and  $N_{pe}$  ( $\lambda=550\text{nm}$ , 900km range) [ $I_i=1000\text{ Wm}^{-2}\text{sr}^{-1}\mu\text{m}^{-1}$ ,  $B_i=2.7\mu\text{Wm}^{-2}\text{sr}^{-1}\mu\text{m}^{-1}$   $R_{diff}=0.25$ ,  $D_b=1.5\text{m}$ ,  $\Delta t=d_{sp}/v_{perp}=2.4\text{ms}$ , pixel  $FOV=72\mu\text{rad}$ ,  $d_{sp}=65\text{m}$ , array  $FOV^1=1.05\text{rad}$ .

Debris $d$ (m)	Aperture $D_b$ (m)	$D_b d \sqrt{R}$	$N_{pe}$ /pixel	$S/B$
1	1.5	0.75	2.45E+06	2.21E+04
0.3	1.5	0.225	2.20E+05	1.98E+03
0.05	1.5	0.038	6.11E+03	5.51E+01
0.01	1.5	0.008	2.45E+02	2.21E+00

Note: This is a 212 Mpixel VIS detector array array, 10cm dia.

**Table 7**

Photon Budget, Active Acquisition:  $S/B$  ( $W=1J$ ,  $\lambda=355\text{nm}$ , 250 km range) [ $I_i=540\text{ Wm}^{-2}\text{sr}^{-1}\mu\text{m}^{-1}$ ,  $B_i=1.5\mu\text{Wm}^{-2}\text{sr}^{-1}\mu\text{m}^{-1}$   $R_{diff}=0.25$ ,  $D_b=1.5\text{m}$ ,  $\Delta t=\Delta z/c=830\mu\text{s}$ , pixel  $FOV=2\mu\text{rad}$ ,  $d_{sp}=0.5\text{m}$ , array  $FOV^1=6\text{mrad}$ ,  $\Delta\lambda=0.2\text{nm}$ ].

Debris $d$ (m)	Laser photons on target/pulse	Signal photons received/pulse	Background photons after filter, splitter, range gate	$S/B$
1	7.15E+18	1.61E+07	1.20E-05	1.34E+12
0.5	1.79E+18	4.02E+06	1.20E-05	3.34E+11
0.2	2.86E+17	6.44E+05	1.20E-05	5.34E+10
0.1	7.15E+16	1.61E+05	1.20E-05	1.34E+10
0.05	1.79E+16	4.02E+04	1.20E-05	3.34E+09
0.02	2.86E+15	6.44E+03	1.20E-05	5.34E+08
0.015	1.61E+15	3.62E+03	1.20E-05	3.01E+08

Note: This is a 9 Mpixel gateable UV detector array array (3000 x 3000 pixels, 12cm dia.)

**Table 8**

Active Acquisition: Spacebased  $S/B$  ( $W=1J$ ,  $\lambda=355\text{nm}$ , 900 km range) [ $I_i=540\text{ Wm}^{-2}\text{sr}^{-1}\mu\text{m}^{-1}$ ,  $B_i=1.5\mu\text{Wm}^{-2}\text{sr}^{-1}\mu\text{m}^{-1}$   $R_{diff}=0.25$ ,  $D_b=1.5\text{m}$ ,  $\Delta t=\Delta z/c=2\text{ms}$ , pixel  $FOV=2\mu\text{rad}$ ,  $d_{sp}=1.8\text{m}$ , array  $FOV^1=6\text{mrad}$ ,  $\Delta\lambda=0.2\text{nm}$ ].

Debris $d$ (m)	Laser photons on target/pulse	Signal photons received/pulse	Background photons after filter, splitter, range gate	$S/B$
1	5.52E+17	9.58E+04	2.89E-05	3.31E+09
0.5	1.38E+17	2.39E+04	2.89E-05	8.28E+08
0.2	2.21E+16	3.83E+03	2.89E-05	1.33E+08
0.1	5.52E+15	9.58E+02	2.89E-05	3.31E+07
0.05	1.38E+15	2.39E+02	2.89E-05	8.28E+06
0.02	2.21E+14	3.83E+01	2.89E-05	1.33E+06
0.015	1.24E+14	2.16E+01	2.89E-05	7.45E+05

Note: This is a 9 Mpixel UV gateable detector array array (3000 x 3000 pixels, 12 cm dia.)

obtained adequate [but much smaller]  $S/B$  ratio using range gating and filtering with a groundbased station, against a daylight sky background, with about the same laser pulse energy per unit of pixel  $FOV$ . Here, we can use a very small pixel  $FOV$  ( $2\mu\text{rad}$ ) because our wavelength is 3 times smaller, and because of the absence of scintillation in space. Table 9 gives the reaction wheel capacity necessary to counter the torque caused by steering the 1000 kg

**Table 9**

Optics Steering Reaction Wheel.

Optics mass $M$	1000	kg
Moment $R$	1	m
Moment of inertia $I$	1000	kg-m
Retarget time	120	s
Accel/decel time	60	s
Total angle	0.52	rad
Angular acceleration	2.9E-4	rad/s <sup>2</sup>
Torque	0.29	N-m
Reaction wheel capacity	17.5	N-m-s

**Table 10**

Typical Impulse Coupling Coefficients (8ns, 1.06  $\mu\text{m}$ ).

Material	$C_{mopt}$ (N/MW)	Refnc
Polyethylene, Kapton®	50	19
Aluminum Alloys	75	20–23
Kevlar®	160	24

active optics system, well within current commercial capability [see Table 9].

#### 4. Laser ablation impulse generation

Anyone who has aligned a pulsed laser beam using a piece of black photo paper has heard and felt the “pop” due to laser momentum transfer. This is one of the few examples of action without reaction on the source.

The figure of merit for pulsed laser ablation is the mechanical coupling coefficient  $C_m$ , which relates the impulse delivered to the target by the laser ablation jet to the laser pulse energy required to produce the jet on its surface:

$$C_m = p\tau / \Phi = p/I N/W. \quad (4)$$

In Eq. (4),  $p$  is the ablation pressure delivered to the target by a laser pulse with intensity  $I$  and duration  $\tau$ , and laser fluence  $\Phi$  ( $\text{J}/\text{m}^2$ )= $I\tau$ .  $C_m$  values for laser ablation are well-known for many materials (Table 10, [21–26]), and are about four orders of magnitude larger than the weak effect of light momentum ( $C_{mh\nu}=2/c=6.7\text{ mN/MW}$ ).

Short-pulse laser ablation creates hot vapor or plasma by the interaction, not new debris.

##### 4.1. Variation with laser parameters

As incident pulsed laser intensity  $I$  increases in vacuum, vapor is formed and  $C_m$  rises rapidly to a peak when laser-produced plasma is formed on the surface, then gradually decreases (Fig. 7, [22]) according to

$$C_m = C_{m0}/(I\lambda\sqrt{t})^{1/4} \quad (5)$$

because more energy is going into reradiation, ionization, and bond breaking than to propulsion.

The parameter  $C_{m0}$  is primarily a function of the average atomic mass  $A$  and charge state  $Z$  in the laser produced plasma above the surface [21], rather than of the surface optical reflectivity at the laser wavelength. This is

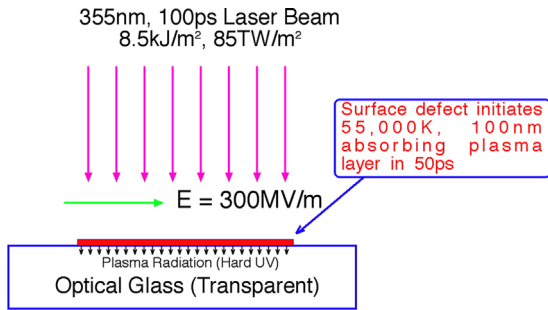


Fig. 6. Surface coupling at high laser intensity.

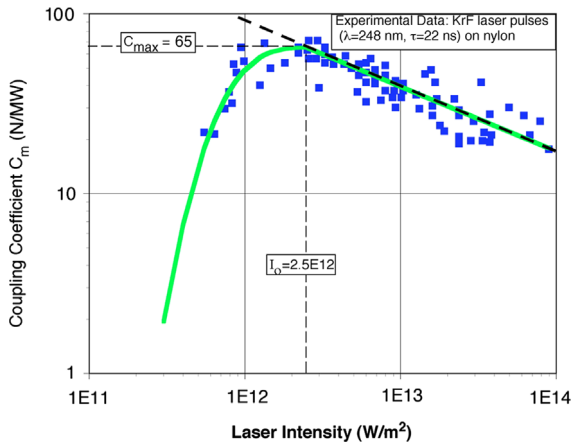


Fig. 7. What optimum coupling means (typical data). Optimum impulse coupling intensity depends on the wavelength and the pulse duration. Plasma regime model is the dashed line.

because the plasma mediates energy transfer from the laser to the surface. For a  $1.06 \mu\text{m}$ , ns-pulse laser incident on a target, the center wavelength reaching the surface can well be in the hard ultraviolet. This is because the plasma is a blackbody radiator, and its temperature in the Fig. 6 example is  $55,000 \text{ K}$ , corresponding to about  $50 \text{ nm}$  wavelength at peak emission. For constant  $A$  and  $Z$ ,  $C_{\text{mo}}$  is a constant. For a singly ionized plasma [ $Z=1$ ] at  $1.06 \mu\text{m}$  wavelength,  $C_{\text{mo}}$  varies from  $75$  to  $200 \text{ N/MW}$  as the target material changes from hydrocarbon with  $A \approx 6$  to iron ore, from  $45$  to  $120 \text{ N/W}$  for  $Z=3$ . For aluminum under these conditions,  $C_{\text{mo}} \approx 420 \text{ N/MW}$ . An approximate relationship for the optimum fluence  $\Phi_{\text{opt}} = I_{\text{opt}}\tau$  where this peak occurs, for a range of metallic and nonmetallic materials, is given by Eq. (6) with a value  $B = 8.5E8 \text{ J/m}^2$  for robust coupling across all materials (about twice the value in Refs. [7,20–22]).

As these examples show, the target material matters only to second order. For example, consider optical glass damage (Fig. 6). On this transparent material, with  $100 \text{ ps}$  pulses, surface defects initiate a hot, high pressure plasma layer in less than  $50 \text{ ps}$ . The plasma is self-regulating so that most of the light is absorbed or reflected. Yet, however hot or reflective, the plasma layer still generates impulse which [22] predicts. Thermal transport to the interior of the substrate occurs after the laser pulse.

We have

$$\Phi_{\text{opt}} \approx B\sqrt{\tau} \text{ J/m}^2 \quad (6)$$

for  $1 \text{ ms} > \tau > 100 \text{ ps}$ . Data shows there is no advantage to using shorter pulses [21]. For example, with an  $8 \text{ ns}$  pulse,  $\Phi_{\text{opt}} \approx 75 \text{ kJ/m}^2$ , while, for a  $100 \text{ ps}$  pulse,  $\Phi_{\text{opt}} \approx 8.5 \text{ kJ/m}^2$ . Peak coupling occurs because of competition between the vapor and plasma regimes. Exact prediction of the intensity where  $C_{\text{m}}$  will be maximized is complicated, depending on the competition between vapor and plasma formation [6,27]. However, we can find the approximate intensity  $I_{\text{opt}}$  for optimum (peak) impulse coupling using Eq. (6) in the form  $I_{\text{opt}}\sqrt{\tau} = \Phi_{\text{opt}}/\sqrt{\tau} = 8.5E8 \text{ W/m}^2\text{s}^{1/2}$  so that

$$(I\sqrt{\tau})_{\text{opt}} = 850\lambda_{\mu\text{m}} \text{ Wm}^{-1}\text{s}^{1/2}. \quad (7)$$

There is no reason to operate elsewhere than at the peak, because this parameter directly affects laser energy and system cost.

Finally, we can substitute Eq. (7) into Eq. (5) to obtain

$$C_{\text{m}} \approx 0.19C_{\text{mo}}/\lambda_{\mu\text{m}}^{1/4} \text{ N/W} \quad (8)$$

#### 4.2. Short pulses and wavelengths

For a particular target material and charge state, Eq. (8) shows an advantage for short wavelengths.

Just going to  $100 \text{ ps}$  pulse duration at  $1.06 \mu\text{m}$  should give  $C_{\text{m}} = 106 \text{ N/MW}$  instead of  $75 \text{ N/MW}$  (Table 10). In fact, Fournier [29] recently measured  $C_{\text{m}} = 155 \text{ N/MW}$  at  $200 \text{ ps}$ ,  $1.06 \mu\text{m}$ . Eq. (3) also tells us that  $\Phi_{\text{opt}} \approx 8.5 \text{ kJ/m}^2$ .

If we also go to  $\lambda = 355 \text{ nm}$ , the 3rd harmonic of Nd, Eq. (8) tells us that we expect  $C_{\text{m}}$ :  $100 \text{ N/MW}$  at  $I\sqrt{\tau} = 300 \text{ W-s}^{1/2}/\text{m}$ , our operating point [Appendix A].

#### 4.3. Pulsed Vs. CW

Table 11 ([7,28,30]), in which the continuous wave (CW) values are based on our calculations using procedures in [6], shows a large coupling and efficiency advantage for pulsed lasers vs. CW lasers for impulse generation on targets.

These calculations are important because, to our knowledge, no published results exist for CW impulse coupling on targets in vacuum. Table 11 shows a factor of 10 improvement in maximum  $C_{\text{m}}$  for pulsed vs. CW lasers. The table shows an unreasonable power

Table 11  
Comparing CW and Impulsive Momentum Coupling.

	CW	100ps pulse (this work)
$C_{\text{mopt}}$ (N/MW)	10	100
Beam Parameter on Target	$10 \text{ MW/m}^2$	$8.5 \text{ kJ/m}^2$ , 32 Hz
Minimum Laser Power Required	$1.45 \text{ MW}$	$40 \text{ kW}$
Thrust Delivered (N)	100	4.0
Relative effectiveness	1	10

Common parameters for this example: Target: aluminum; Wavelength:  $1.06 \mu\text{m}$ ; Range:  $500 \text{ km}$ ; Illumination spot diameter at range:  $0.43 \text{ m}$ .

(1.5 MW) for a CW laser to illuminate a 43 cm spot with sufficient intensity to generate good impulse coupling. Looked at another way, CW lasers cannot reach the required intensity for efficient coupling to targets at the ranges involved without a very small illumination spot size, requiring an unacceptably large mirror. Other disadvantages of CW target heating are that slow heating and decay of tumbling debris will normally give an ablation jet whose average momentum contribution cancels itself as the target rotates. CW heating also causes messy melt ejection (as with a welding torch) rather than clean jet formation, adding to the debris problem, contrary to the behavior of pulsed ablation.

4.4. Relationship among laser parameters for optimum impulse on target

In order to calculate deliverable  $(I\lambda\sqrt{\tau})_{opt}$  on a target at range  $z$ , we first need to consider beam spread due to diffraction. If beam quality is held constant, short wavelengths focus better, proportionally to wavelength and range but inversely with effective aperture diameter  $D_{eff}$ , because of diffraction. The product of the effective launched beam diameter  $D_{eff}$  and beam spot diameter  $d_s$  at the target is

$$d_s D_{eff} = a M^2 \lambda z, \tag{9}$$

where  $M^2$  is the beam quality factor (1 is perfect) and  $D_{eff}$  is the effective illuminated beam diameter associated with the laser station output aperture with diameter  $D_b$  for calculating diffraction, and depends on beam radial profile. For example, if we use a 6th-order hypergaussian radial intensity profile  $I(r)/I_0 = \exp(-r/r_0)^6$ , with corrected beam quality  $M^2 = 2.0$  (Strehl ratio  $S = 1/M^2 = 0.25$ ), we find  $D_{eff}/D = 0.9$  and  $a = 1.7$  [31].

The constant  $a$  regulates diffraction: for the classical Airy pattern,  $a = 2.44$ .

The product  $WD_{eff}^2$  required to deliver fluence  $\Phi$  to the target is given by [7]

$$WD_{eff}^2 \frac{\pi M^4 a^2 \lambda^2 z^2 \Phi}{4T_{eff}} = \frac{\pi M^4 a^2 \lambda^2 z^2 B \sqrt{\tau}}{4T_{eff}} \tag{10}$$

In Eq. (10),  $W$  is laser pulse energy (J) on the target and the effective transmission from the L'ADROIT aperture to the target  $T_{eff}$  is the product of all system losses, including apodization, obscuration and atmospheric transmission.

Eq. (10) shows that the required pulse energy  $W$  increases less than linearly with pulse duration and quadratically with range in this case. Inverting Eq. (10), the delivered fluence given the other parameters is

$$\Phi = \frac{4WD_{eff}^2 T_{eff}}{\pi M^4 a^2 \lambda^2 z^2} \tag{11}$$

Eq. (12) gives velocity change per laser pulse.

$$\Delta v_{||} = \eta_c C_m \Phi / \mu. \tag{12}$$

This formulation is important. It allows us to calculate velocity change along the track for one or many small debris of a given  $\mu$ , of whatever size, if they are in the beam and smaller than the beam at their location. In Eq. (12),  $\eta_c$  is an impulse transfer efficiency factor which

includes the combined effects of improper thrust direction on the target, target shape effects, tumbling, etc. in reducing the laser pulse efficiency in producing the desired vector velocity change antiparallel to the target track. For large debris, we use the same formulation, but artificially increase  $\mu$  to get the desired mass – which is always 1000 kg for our analysis, and require that the target is always larger than the beam at its location.

For small debris, we choose  $\mu = 1 \text{ kg/m}^2$  as typical [32]. Some pieces are heavier and will take longer to re-enter than the typical case, and some are lighter.

5. System performance

5.1. System operation

Pulse duration is constant. Pulse energy can easily be varied from just 1J for locating targets to ~1 kJ for creating plasma, and energy (high to low) and repetition rate (low to high) is varied as the target approaches, keeping average power roughly constant (Fig. 8).

A 1–2 min retargeting interval lets the laser cool off in heat capacity mode, although we may still use 1 J pulses for active acquisition while it is cooling (Tables 12,13). The passive system detects targets at 500 or 900 km range and tells the active system where to change its pointing direction during the retargeting interval. For small targets, we can detect as many as 80/min at 500 km range, and 5/min for the large ones at 900 km because of the larger sample volume – so we can let a lot of them go by. Then, we pick an optimum target when the laser is cool and shoot it. More than likely, there are 1 to 3 of them just located in the box where we want them [250 +/- 75 km or 600 +/- 300 km] at the moment we 'are ready to shoot (Tables 3,4), and the computer will have stabilized pointing by that time.

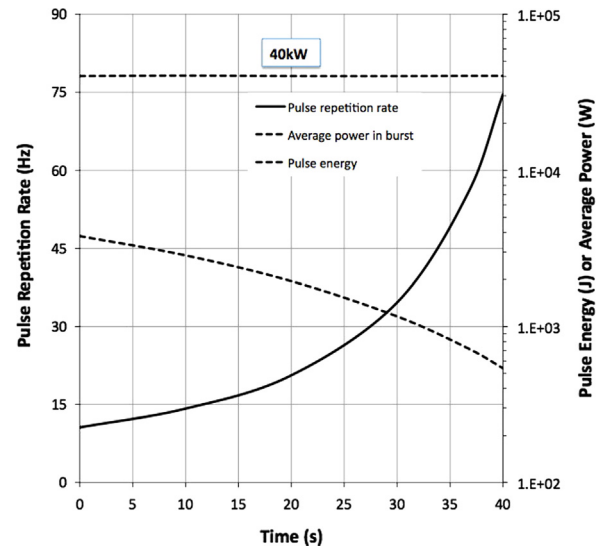


Fig. 8. As pulse energy and repetition frequency vary for large target reentry, power during the laser burst is constant.

**Table 12**

Small Target Re-entry, 355 nm Station in Polar Orbit [Generic Target].

Target and station parameters		Optical system parameters	
Total Number in 560–960 km Altitude Band	100 k	Typical Pulse Energy (J)	380
Mass [nonspecific target] (kg)	< 0.038	Pulse Repetition Frequency (Hz)	56
Range z (km)	250 ± 75	Laser output power (burst, kW)	21
Operating Fraction [day/night] (%)	50	Wavelength $\lambda$ (nm)	355
Number of Passes for small debris Re-entry	1	Pulse Length $\tau$ (ns)	0.1
Time to Re-enter one debris (Head-on, s)	10	Spot Size on Target $d_{sp}$ (m)	0.22
Recovery/Retargeting interval (s)	120	Fluence on Target (kJ/m <sup>2</sup> )	8.5
Primary Mirror Diameter (m)	1.5	Beam Quality Factor	2.0
Push Efficiency $\eta_c$	0.50	Target Typical Crossfield Rate (mrad/s)	30
Momentum Coupling Coefficient (N-s/MJ)	99	Detection Rate (/min)	15
<b>Time to Remove All Targets (mo.)</b>	<b>4.6</b>	<b>Time Average Laser Power (kW)</b>	<b>1.8</b>
<b>Cost per small Object Removed (\$)</b>	<b>310</b>	Target Removal Rate (/operating hour)	30
<b>Cost per kg Removed (\$)<sup>a</sup></b>	<b>8</b>	Acquisition Field of View (degrees)	60
		Launch cost fraction (%)	31

<sup>a</sup> Cost is prorated to time per target. Cost model is approximate and proprietary to Photonic Associates, LLC, based on [11].

**Table 13**

Large Target Raise/Lower 40km, 355nm Station in Polar Orbit [Generic Target].

Target and station parameters		Optical system parameters	
Total Number in 560–960 km Altitude Band	2 kmk	Typical Pulse Energy (J)	1950
Mass [nonspecific target] (kg)	1000	Pulse Repetition Frequency (Hz)	21
Range z (km)	600 ± 300	Laser output power (burst, kW)	40
Operating Fraction [day/night] (%)	100	Wavelength $\lambda$ (nm)	355
Number of Passes for Raising/Lowering	625	Pulse Length $\tau$ (ns)	0.1
Shine Time per Interaction (s)	40	Spot Size on Target $d_{sp}$ (m)	0.50
Recovery/Retargeting Interval (s)	60	Fluence on Target (kJ/m <sup>2</sup> )	8.5
Primary Mirror Diameter (m)	1.5	Beam Quality Factor	2.0
Push Efficiency $\eta_c$	1.0	Target Typical Crossfield Rate (mrad/s)	12
Momentum Coupling Coefficient (N-s/MJ)	99	Detection Rate (/min) [much larger test vol.]	5
<b>Time to remove all targets (yrs)</b>	<b>4</b>	<b>Time average laser power (kW)</b>	<b>16</b>
<b>Cost per target lowered/raised (k\$)</b>	<b>280</b>	Target $\Delta v_{  }$ /pass (cm/s)	8.3
<b>Cost per kg removed (\$)<sup>a</sup></b>	<b>280</b>	Acquisition field of view (degrees)	60
		Launch cost fraction (%)	18

<sup>a</sup> Cost is prorated to time per target. Cost model is approximate and proprietary to Photonic Associates, LLC, based on [11].

In Fig. 4, only the beam projection Cassegrain telescope is steered. In order to avoid aberration, this requires a periscope arrangement of two flat mirrors inside the laser system to rotate and tilt the laser beam along with the telescope. The reaction wheel and steering components will cause vibration onboard the spacecraft. The 0.5  $\mu$ rad pointing accuracy implied by Tables 3 and 4 is achieved by precision piezoelectric transducers tilting the first of these mirrors over a  $\mu$ rad range against a combination of fixed star and angular accelerometer references with a 1 kHz feedback loop bandwidth.

### 5.2. Small target re-entry

Table 12 shows performance for an optimized space-based UV laser system in producing small target re-entry.

Here, our goal is single interaction re-entry, because post-shot tracking of the small objects is difficult. For this reason, we provide bursts of laser power sufficient to re-enter most of the small targets in a ten second interaction. In one interaction, we provide 236 m/s  $\Delta v$ , which is

sufficient for re-entry. It is interesting that this task can be completed for 100 k targets in a little over four months, almost immediately removing the objects which communicate the breakup instability. In small target mode, the duty factor is 50% because we need daylight to locate targets.

### 5.3. Large target raising/lowering

For large targets  $\sim$ 1000 kg, we can only make small velocity changes in one interaction [Table 13], so we assume groundbased tracking assistance to relocate a specific object after an interaction and give us 100% duty factor. Typical  $\Delta v$  per interaction is 8.3 cm/s, so 625 interactions are required to provide 43 m/s  $\Delta v$  necessary to raise or lower the 1000 kg object by 40 km (see Section 3.2) It will take about 4 years to complete this operation on 2000 one-ton objects, so we consider the majority of system cost to be borne by this application. We note that both jobs can be done with a 2–15 kW average power laser capable of 20–40 kW bursts lasting 10–40 s.

We assume the total system mass in orbit is 10,000 kg. All costs are based on an assumed total system cost of 560 M\$, amortized over four years' operation, only 10% of which is devoted to the small targets. This figure is assumed to include 410 M\$ for the satellite, 145 M\$ for launch and 5M\$ for the cost of operations over the period. A Falcon 9 launcher would be suitable.

### International cooperation

The most salient problem for L'ADROIT is not technical, but political. Designing, building and operating a laser system in space will require international cooperation to apply the best ideas, as well as to avoid concerns that it is actually a weapon system. Also, cooperation in its operation will be needed to get permission for its use to remove specific debris objects.

### Conclusions

We have reviewed a novel debris-clearing system using an orbiting short-pulse UV laser system with only tens of kW average power, which avoids the perceived risks of pulsed laser debris removal.

We showed that our L'ADROIT configuration is more agile and less costly than mechanical debris removal techniques. It can handle tumbling objects, difficult for mechanical systems. It is the only approach that can deal with both small and large debris objects, and it will work on multi-ton objects. In general, we conclude that the cost of removing a single piece of small debris is less than 1 k\$. To raise or lower a generic large target, we expect a cost to be of order 280 k\$.

A spacebased UV laser system has special advantages in range, rate of acquisition and interaction geometry that drive the estimated cost to a low level, compared to groundbased systems. The incremental cost of putting a L'ADROIT system in space is typically less than a 20% component of the total system cost.

This system can also be used to defend specific high-value assets from an anticipated debris encounter.

### In Memoriam

This work is dedicated to Dr. Victor George (1938–2014), an early member of the laser program at Lawrence Livermore National Laboratory, who supported laser space debris removal concepts for many years.

### Acknowledgments

The author gratefully acknowledges Wolfgang Schall [33] for introducing the concept of spacebased laser active debris removal in this journal 23 years ago, Joe Carroll, Tether Systems, Inc. for many discussions during this work, and Christophe Bonnal at CNES for his continuing patience and interest in this project.

### Appendix A. Variation of Impulse Coupling Coefficient with Materials

To answer questions about the extent to which the nature of the material matters in laser plasma formation, Fig. A1 shows the variation of  $C_m$  with  $l\lambda\sqrt{\tau}$  for a large number of nonmetallic materials in 13 data sets, together with the predictions of our theoretical model [22,23]. Similar results were obtained for aluminum and its alloys using nine additional data sets in [22]. In that work, data were modeled in four cases with specific Saha equations giving ionization state  $Z$  vs. laser-induced plasma temperature (solid and dashed lines). Changes in the model prediction for  $C_m$  vs  $l\lambda\sqrt{\tau}$  in each of the cases are due to changes in the predicted  $Z$ , which is a function of temperature. The optimum value of  $l\lambda\sqrt{\tau}$  is the smallest value that produces the largest  $C_m$ . The value that we use for 355 nm and 100 ps in this work,  $C_m=100$  NMW, is conservative, because shorter wavelength and pulse duration than the Fournier datum each give higher  $C_m$  than his value, even though we operate slightly above optimum intensity for robust coupling on all materials. Data is not available for all materials at all wavelengths, intensities or pulse durations. Our theoretical model matches the variation of  $C_m$  with the parameter  $l\lambda\sqrt{\tau}$  for a wide variety of materials in the plasma regime for wavelengths from 248 nm to 10.6  $\mu\text{m}$  and pulse durations from 100 ps to 1 ms, and shows that  $C_m$  varies no more than a factor-of-2 above or below the model predictions for all these materials, starting from first principle calculations. These include aluminum and polymers such as kapton (a polymer like data series m in the Figure) – the components of

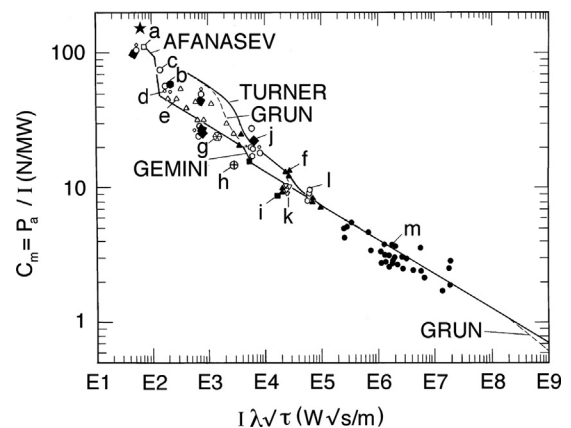


**Fig. A1.** Published data for impulse coupling coefficient on nonmetallic materials which might be found in space debris, compared with our theoretical model [19], vs. the parameter  $l\lambda\sqrt{\tau}$ . The modeled cases were: UV short pulses ("TURNER," 248 nm, 22 ns), midspectrum short pulses ("GRUN," 1.06  $\mu\text{m}$ , 5 ns), midspectrum long pulses ("AFANASEV," 1.06  $\mu\text{m}$ , 1.5 ms), and infrared long pulses ("GEMINI," 10.6  $\mu\text{m}$ , 1.8 ms). Materials are: (a): Ebonite rubber. (b, i): Carbon. (c): Silica phenolic. (d): Vamac rubber. (e): Buna-n rubber. (f): Kevlar epoxy. (g, h): Grafoil. (j): Carbon phenolic. (k): Graphite epoxy. (l): Carbon phenolic. (m): C-H foils. References for the data are found in [19]. [Used by permission, copyright 1988, American Institute of Physics]. As a comparison, recent data by Fournier [29] for 200ps pulses on Al at 1.06  $\mu\text{m}$  give  $C_m=155\text{N/MW}$  at  $l\lambda\sqrt{\tau}=80\text{W}\sqrt{\text{s}}/\text{m}$  (\*). This data point agrees well with our model and, because of Eq. (8), we expect a 30% larger value than Fournier's at 355nm.

multilayer insulation (MLI) – all of which fit the model to with factors of well. Physically, the parameter  $I\sqrt{\tau}$  is intermediate between a fluence  $I\tau$  and an intensity  $I$ , and is the governing parameter in one dimensional heat transfer problems. The parameter  $I\lambda\sqrt{\tau}$  is the key parameter governing  $C_m$ .

## Appendix B. electrical and optical systems

### B.1. laser

The laser is a laser-diode-pumped solid state oscillator-amplifier. We assume the amplifier medium is Nd:YAG (neodymium-doped yttrium aluminum garnet matrix), or Nd:glass. It could be Yb:YAG. The latter has a lower energy defect and so creates less waste heat. This is because its pump band is almost the same as the lasing wavelength, which is not true for Nd:YAG. However, this choice leads to trickier laser design, including cryogenic operation. Energy storage density is about 0.66 kJ/liter in Nd:glass [34], and with a density of 2.8 kg/liter, perhaps 10 kg for the entire laser amplifier medium. By far the majority of system mass will be due to pump diode bars, their power supplies, solar arrays, and heat dissipation equipment. In the Lawrence Livermore Laboratory LIFE laser design, a diode-pumped Nd:glass device intended to produce 18 Hz, 7 kJ, 355 nm

pulses with several ns pulse duration for a fusion reactor (130 kW average power, more than 8 times what we require), optical component mass would have been about 10,000 kg, and occupy about 31m<sup>3</sup> [35,36]. The overall electrical to optical efficiency  $\eta_{e-o}$  of the Nd:glass LIFE laser design at 355 nm was 21%. Improvements since then have increased this number. For example, the LIFE design uses 75% for frequency conversion efficiency to the third harmonic at 351 nm, whereas 85% is now possible [37]. Laser diodes can now be 70% rather than 66% efficient [37]. Total transport efficiency is taken as 88%, but it can be very near 100% in a small system such as ours. Taking all these incremental factors together gives a net  $\eta_{e-o} = 32\%$ .

### B.2. optical damage Thresholds

Using [37] we have estimated the damage threshold fluences for fused silica glass shown in Table B1 for our case at several wavelengths.

In the Table, we have taken the [38] value for 1ns pulses and reduced it by  $\sqrt{10}$  to estimate damage threshold at 100 ps. Fused silica is representative of optical materials in the laser system. The table shows the main reason we jettisoned our original 266 nm design for this system: damage threshold at the 4th harmonic is 2 times less than for the 3rd. With 40 cm diameter, our most stressed high power beam components (zoom lens, convex mirror) operate comfortably a factor of 4 below the optical damage limit. At Brewster's angle, the laser amplifier disks will operate at an additional factor of 1.8 below damage threshold.

### B.3 system power budget

Using best current figures, we estimate overall energy budget and solar array performance as shown in Table B2. As a benchmark for solar array parameters, we note that the 12-year-old International Space Station solar array

**Table B1**  
Fused silica damage Thresholds  $\Phi_d$   
(J/cm<sup>2</sup>) at 100 ps.

$\lambda$ (μm)	$\Phi_d$
1065	11
532	8
355	7
266	3

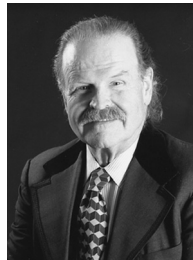
**Table B2**  
Estimated L'ADROIT system parameters.

Parameter	Value	Unit	Reference
Laser output at 3rd harmonic (355 nm)	15	kW	
1st to 3rd harmonic conversion efficiency	0.85		[37]
Diodes to 1st harmonic conversion efficiency	0.53		[36,39,40]
Laser diode electrical to optical (e-o) efficiency	0.70		[41]
Overall laser e-o efficiency	0.32		
Resulting laser electrical input	48	kW	
Heat removal system	15	kW	
Reaction torque motor	3	kW	
Data and miscellaneous	1	kW	
Total system electrical power requirement	67	kW	
Solar array mass/area	0.85	kg/m <sup>2</sup>	[42]
Solar array power/area	0.27	kW/m <sup>2</sup>	[42,43]
Resulting solar array area	247	m <sup>2</sup>	
Resulting solar array mass	210	kg	
Passive detection mirror and mount mass	790	kg	
Active mirror system and steering	1000	kg	
Laser system mass including laser diodes	2500	kg	
Electrical system mass including batteries	2500	kg	
Cooling system mass	1500	kg	
Spacecraft, thrusters and fuel mass	1500	kg	
Total system mass	10,000	kg	

design generates 92 kW [38]. Batteries store energy for bursts in heat-capacity mode.

## References

- [1] Gravity, movie 2013 produced by Esperanto Filmoj and Heyday Films, directed by Alfonso Cuarón.
- [2] D. Kessler, B. Cour-Palais, Collision Frequency of Artificial Satellites: The Creation of a Debris Belt, *J. Geophys. Res.* 83 (1978) 2637–2646.
- [3] J. Henderson, S. Nikolaev, et al., Intelligent sensor tasking for space collision mitigation, *Proc. SPIE* 7691 (2010) 76910L.
- [4] L. Simms, V. Riot, et al., Optical payload for the STARE pathfinder mission, *Proc. SPIE* 8044 (2011) 804406.
- [5] P. Brudieu, B. Lazare, French Policy for Space Sustainability and Perspectives, in: Proceedings of the 16th ISU Symposium on Space Activities, Strasbourg, 2012.
- [6] P. Maier, et al. ISU Team Project: an Integral view on space debris mitigation and removal, In: Proceedings of the 6th European Conference on Space Debris, Darmstadt, 22–25 April 2013.
- [7] C. Phipps, et al., Removing orbital debris with lasers, *Adv. Space Res.* 49 (2012) 1283–1300.
- [8] C. Phipps, Catcher's Mitt as an alternative to laser space debris mitigation, *AIP Conf. Proc.* 1278 (2010) 509–514.
- [9] C. Bonnal, High level requirements for an operational space debris deorbit. In: Proceedings of the NASA/DARPA International Conference on Orbital Debris Removal, Chantilly, VA, 2009.
- [10] J. Mason, J. Stupl, et al., Orbital Debris Collision Avoidance, arXiv:1103.1690v1 [physics.space-ph], 2011.
- [11] J. Campbell, Project ORION: Orbital Debris Removal Using Ground-Based Sensors and Lasers, NASA Marshall Spaceflight Center Technical Memorandum 108522, 1996.
- [12] C. Bombardelli, H. Urrutxua, M. Merino, E. Ahedo, J. Peláez, L. Summerer, A Plan to Deorbit Envisat, in: Proceedings of the 2nd European Workshop on Active Debris Removal, Paris, 2012.
- [13] V. Kirchoff, D. Pinheiro, D., Wavelength dependence of aerosol optical thickness in the UV-B band, *Geophys. Resch. Lett.* 29 (2002) 58-1–58-4.
- [14] Klinkrad H., Space Debris, Models and Risk Analysis, Springer Praxis (2006) and updates provided by H. Krag (2014).
- [15] H. Kogelnik, T. Li, Laser beams and resonators, *Appl. Opt.* 5 (1996) 1550.
- [16] E. Köse, R. Perline, Double-mirror catadioptric sensors with ultra-wide field of view and no distortion, *Appl. Opt.* 53 (2014) 528–536.
- [17] C. Phipps, S. Bodner, J. Shearer, Reflective optics system for uniform spherical illumination, *Appl. Opt.* 14 (1975) 985–991.
- [18] C.W. Allen, Astrophysical Quantities, Athlone, London, 1973.
- [19] W.L. Wolfe, G.J. Zissis, The Infrared Handbook, Office of Naval Research, Washington, D.C., 1978.
- [20] J.P. Reilly, The Infrared Handbook, Office of Naval Research, Campbell, 1996.
- [21] C. Phipps, *Appl. Surf. Sci.* 252 (2006) 4836–4844. (2006).
- [22] C. Phipps, et al., Impulse Coupling to Targets in Vacuum by KrF, HF and CO<sub>2</sub> Lasers, *J. Appl. Phys.* 64 (1988) 1083–1096.
- [23] C. Phipps, M. Birkan, et al., Laser ablation propulsion, *J. Propuls. Power* 26 (2010) 609–637.
- [24] P. Combis, P. B. B. Cazalis, J. David J. A. Froger A. M. Louis-Jacquet, M. B. B. Meyer, G. Nierat G. A. Saleres A. G. Sibille G. G. Thiell G., F. Wagon F, Low fluence laser–target coupling, *Laser Particle Beams* 9 (1991) 403–420.
- [25] A. Saleres, B. Cazalis, P. Combis, J. David, B. Meyer, G. Nierat, G. Sibille, G. Thiell, F. Wagon, Couplage Thermique et Mécanique dans L'interaction Laser-Matière a Éclairément Modéré, CEA Limeil-Valenton report 4<sup>ème</sup> Trimestre, 1992.
- [26] Yu.V. Afanas'ev, N.G. Basov, O.N. Krokhin, N.V. Morachevskii, G. V. Sklizkov, Gas-dynamic processes in irradiation of Solids, *Sov. Phys. Tech. Phys.* 14 (1969) 669–676.
- [27] C. Phipps, J. Luke, D. Funk, D. Moore, J. Glownia, T. Lippert, Laser impulse coupling at 130fs, *Appl. Surf. Sci.* 252 (2006) 4838–4844.
- [28] C. Phipps, An alternate treatment of the vapor-plasma transition, *Int. J. Aerosp. Innov.* 3 (2011) 45–50.
- [29] K. Fournier, LASNEX calculations of laser-coupling coefficients for Al targets, Lawrence Livermore Laboratory presentation UCRL-Pres 226849 (2006) 29.
- [30] C. Phipps, A laser-optical system to re-enter or lower low Earth orbit space debris, *Acta Astronautica* 93 (2014) 418–429.
- [31] C. Phipps, S. Thomas D. Watkins, Effect of Nonlinear Refraction on Beam Brightness in Laser Fusion Applications, *Proc. Intl. Conf. on Lasers'79*, 1980.
- [32] H. Klinkrad, *ibid.* 2006, Fig. 3.3, p. 70.
- [33] W. Schall, Orbital debris removal by laser radiation, *Acta Astronaut.* 24 (1991) 343.
- [34] W. Koehnner, *Solid State Laser Engineering*, Springer Verlag, 2006.
- [35] K. Fournier, Lawrence Livermore National Laboratory (2014), private communication.
- [36] A. Bayramian, A. Erlandson, Comparison of Nd:phosphate glass, Yb:YAG and Yb:S-FAP laser beamlines for laser inertial fusion energy, LLNL-PRES-581113, 2012. [https://www.lasers.llnl.gov/workshops/hec\\_dpssl\\_2012/pdf/9-13-12/A.Erlandson.pdf](https://www.lasers.llnl.gov/workshops/hec_dpssl_2012/pdf/9-13-12/A.Erlandson.pdf).
- [37] D. Neely, Rutherford Appleton Laboratory, UK (2014), private communication.
- [38] <http://www.esa.int/esapub/br/br202/br202.pdf>.
- [39] N. Kuzuu, et al., Laser-induced bulk damage of various types of silica glasses at 532nm and 355nm, *Japanese J. Appl. Phys* 43 (2004) 2547–2548.
- [40] A. Bayer, B. Köhler, A. Noeske, M. Küster, D. Irwin, S. Spatterson, J. Biesenbach, J. Scalable and modular diode laser architecture for fiber coupling that combines high-power, high-brightness and low weight, paper 2014-02-04, Photonics West, 2014.
- [41] J.J. Noekum, Overview on New Diode Lasers for Defense Applications, in: Proceedings of the SPIE Europe Security and Defense, 2012 (<http://spie.org/x4304.xml>).
- [42] BEPI-COLUMBO: Haag, M. (2006) Lightweight fiber-coupled diode laser pump module for the BeipColumbo laser altimeter. In: Proceedings of the 2nd ESA-NASA Working Meeting on Optoelectronics, Noordwijk, Netherlands.
- [43] N. Fatemi, et al. (2000). Solar array trade studies between very high efficiency multi-junction and Si space solar cells. *Proc. 28<sup>th</sup> IEEE PVSC*, Anchorage, Alaska.



**Claude Phipps** earned B.S. and M.S. degrees from the Massachusetts Institute of Technology, and a Ph.D. from Stanford University in 1972. He worked in the Inertial Confinement Fusion Program at Lawrence Livermore Laboratory and, from 1974 to 1995, in the Advanced Optical Systems Group at Los Alamos National Laboratory (LANL). There, he conducted a research program on mechanical and thermal coupling of pulsed lasers to targets using high-energy-laser facilities in the United States and United Kingdom, and developed a model for vacuum laser impulse prediction. From 1994 to 1995, he was Associate Director of the Alliance for Photonic Technology at LANL. In 1995, he formed Photonic Associates, which is devoted to applications of laser space propulsion. He is the author of 124 peer-reviewed papers, 120 conference presentations including 40 invited talks and a keynote, has contributed to two textbooks on laser ablation phenomena, and has organized and chaired eleven symposia on high-power laser ablation and beamed energy propulsion.